In vivo Ca²⁺ imaging of astrocytic microdomains reveals a critical role of the amyloid precursor protein in mitochondria network stability

Elena Montagna[1,2,3,7], Sophie Crux[1,2,3,7], Manja Luckner[4], Julia Herber[1,5], Alessio V. Colombo[1], Sabina Tahirovic[1], Stefan F. Lichtenthaler[1,3,5,], Gerhard Wanner[4], Ulrike Müller[6], Carmelo Sgobio[1,*], Jochen Herms[1,2,3,*]

1 German Center for Neurodegenerative Diseases (DZNE), Munich, Germany
2 Center for Neuropathology and Prion Research, Ludwig–Maximilians-University, Munich, Germany
3 Munich Cluster of Systems Neurology (SyNergy), Ludwig-Maximilians-University, Munich, Germany
4 Department Biology I, Biocenter, Ludwig-Maximilians-University Munich, Planegg-Martinsried, Germany
5 Neuroproteomics, School of Medicine, Klinikum rechts der Isar and Institute for Advanced Study, Technische Universität München, Munich, Germany
6 Department of Bioinformatics and Functional Genomics, Institute of Pharmacy and Molecular Biotechnology, Heidelberg University, Heidelberg, Germany
7 These authors contributed equally to this work.
Correspondence should be addressed to J.H. (jochen.herms@med.uni-muenchen.de) or C.S. (carmelo.sgobio@dzne.de)

The investigation of amyloid precursor protein (APP) has been mainly confined to its neuronal functions, whereas very little is known about its physiological role in astrocytes. Astrocytes exhibit a particular morphology with slender extensions protruding from somata and primary branches. Along these fine extensions, spontaneous calcium transients occur in spatially restricted microdomains. Within these microdomains mitochondria are responsible for local energy supply and Ca²⁺ buffering. Through two-photon *in vivo* Ca²⁺ imaging, we report significant decrease in the density of active microdomains, frequency of spontaneous Ca²⁺ transient activity and slower Ca²⁺ kinetics in mice lacking APP. Moreover, we observed severe structural fragmentation of the mitochondrial network that was dependent on the presence of APP. Our results highlight a substantial role of APP in the modulation of Ca²⁺ activity in astrocytic microdomains whose precise functioning is of significance for the reinforcement and modulation of the neural network. Due to the involvement of APP in Alzheimer's disease (AD), our results provide novel evidence on APP physiological functions, important for the development of efficacious AD treatments.

Introduction

The physiological functions of APP have been the subject of intensive studies, mainly due to the involvement of APP and its cleavage products in Alzheimer's disease (AD) (1). It is described that APP isoforms are distributed in a cell-specific manner, with the Kunitz protease inhibitor (KPI)-containing isoforms (751,770) predominantly occurring in astrocytes (2). Although its astrocytic expression is proven (2,3), the physiological role of APP in these cells remains largely unknown. Astrocytes are important neuronal partners with highly branched processes contacting up to 100.000 synapses from multiple neurons (4), refining neuronal networks, and regulating uptake of neurotransmitters and ion homeostasis (4,5). Astrocytes do not fire action potentials but display spontaneous as well as pharmacologically evocable intracellular increase of Ca²⁺ transients, necessary to modulate gliotransmitter release and thus neuronal activity (6,7). The distal appendages of astrocytes present repeated structures, termed microdomains, which show spontaneous increase of intracellular Ca²⁺ levels. Mitochondria are localized inside of microdomains, thus suggesting that microdomains are metabolically independent (8). Several

43   evidences ascribe a pivotal role in modulating Ca^{2+} transients to mitochondria (9). Specifically, the close

44   apposition of mitochondria to the reticulum endoplasmaticum (ER) has been shown to be necessary for an

45   efficient Ca^{2+} homeostasis within astrocytic microdomains (10,11).

46   The presence of APP has been proven to be important for Ca^{2+} dependent activities in astrocytes. Recent

47   *in vivo* findings in APP knockout (APP-KO) mice revealed an alteration in the homeostasis of D-serine, a

48   gliotransmitter released in response to elevated Ca^{2+} levels (12). Congruently, previous studies on cultured

49   astrocytes of APP-KO mice revealed altered Ca^{2+} and ATP homeostasis (13,14), both hallmarks of altered

50   mitochondrial function (15). AD-related studies identified mitochondria-associated ER membranes

51   (MAM) as sites of APP cleavage product C99 (the 99-amino acid at APP carboxyl-terminal) accumulation

52   which interferes with the mitochondrial respiratory chain (16). Additionally, the KPI domain of APP,

53   which is predominantly expressed in astrocytes, has been shown to be important for mitochondrial

54   localization and function (17). More specifically, APP localizes at the translocase of the outer

55   mitochondrial membrane (TOMM) complex, where it affects the import of nuclear encoded proteins into

56   mitochondria (18). Intriguingly, this mechanism appears disrupted in AD (18–20), where APP tends to

57   accumulate around TOMM complexes. However, the understanding of the physiological function of APP

58   interacting with mitochondria needs further investigations.

59   The aim of this work was to investigate the effects of the depletion of APP in astrocytes, starting from *in*

60   *vivo* microdomain calcium imaging followed by the study of mitochondrial networks in astrocytic cultures

61   from APP-KO mice.

62   The analysis of Ca^{2+} transients along the fine processes of astrocytes was conducted by adeno-associated

63   viral vector (AAV) delivery of astrocytically expressed membrane-bound genetically encoded Ca^{2+}

64   indicator (AAV-lck-GCaMP6f) into the somatosensory cortex of APP-KO and wild type animals and

65   monitored spontaneous Ca^{2+} activity by *in vivo* two-photon imaging. The analysis of the Ca^{2+} fluctuations

66   demonstrated that lack of APP significantly affects Ca^{2+} transients in the microdomains of astrocytes.

67   Subsequently, a cell culture approach allowed us to selectively isolate astrocytes from neurons and other

68   cell types and revealed a fragmented mitochondria phenotype in APP-KO astrocytes.

69

70 Results

71 Distribution and activity profile of astrocytic microdomains are reduced in APP-KO
72 animals

73   In order to investigate spontaneous Ca^{2+} fluctuations along the fine astrocytic processes, we injected

74   AAV.Pzac2.1gfaABC1Dlck-GCAMP6f (AAV-lck-GCaMP6f) into the somatosensory cortex of three

75   months old WT and APP KO mice (Figure 1A). At the same time, mice were co-transduced with

76   AAV.GfaABC1DcytotdTomato.SV40 (AAV.Gfacyto.tdtomato) (Figure 1A) to confirm the astrocyte-

specific expression of the Ca^{2+} indicator AAV-lck-GCaMP6f (Figure 1A). Notably, the AAV-lck-GCaMP6f expression is detected within fine protrusions of astrocytes, perfectly suitable for the investigation of astrocytic Ca^{2+} transients (ASCaTs). Two-photon *in vivo* Ca^{2+} microscopy was conducted in the somatosensory cortex of mice kept under isoflurane anesthesia. Respiratory rate, temperature and oxygen levels in the blood were constantly monitored and isoflurane concentration was modified accordingly to guarantee equal depth of anesthesia between mice (Figure 1B). Imaging series of 5 min were acquired with a sampling rate of 4.17 Hz. For the identification of active microdomains and their calcium transient activity analysis, we applied a protocol adapted from Agarwal et al. (11). The analysis was performed on single focal 60 x 60 µm images, as a time stack image series. As described in more detail in the method section, we low-pass filtered the time stack for background noise reduction at first. Then, a heat map of ASCaTs activity was generated and an arbitrary threshold (average of the overall activity plus three standard deviations) was used to identify active microdomains. The analysis procedure generated a mask of microdomains assigned regions of interest (ROIs) that was applied on the raw image time series. Subsequently, the traces of single ROIs were extracted and single ASCaTs were isolated and analyzed in terms of frequency, event size and kinetics. All ROIs with 1.5-fold fluorescence intensity above the baseline noise were considered as active domains.

From the analysis of ROIs/microdomains distribution (Figure 2A,B), we detected that active microdomain density was reduced by ~50% in APP-KO compared to WT astrocytes (Figure 2C). Moreover, a substantial increase of the average microdomain area in APP-KO astrocytes (~25% compared to WT) (Figure 2D) was also confirmed by the analysis of the frequency distribution of the microdomain size depicted (Figure 2E), suggesting that APP-KO astrocytes have less small microdomains. Finally, Ca^{2+} activity analysis based on the traces extracted from active microdomains showed a reduction of ~45% in ASCaTs frequency in APP-KO astrocytes compared to WT (Figure 2F).

These results indicate that APP depletion is responsible for the reduction of active microdomains and the frequency of spontaneous and locally restricted Ca^{2+} transients occurring in the fine processes of astrocytes *in vivo*.

APP-KO exhibits slow ASCaTs kinetics within their active microdomains.

After confirming that the population of microdomains was not only smaller but also displayed less ASCaTs in APP-KO, we focused on the study of the kinetics as functional analysis of the local Ca^{2+} homeostasis. From the extracted traces, at first, we considered both single peaks of calcium increase and extrapolated peaks from burst-like transients, which occasionally occurred as multiple set of single subsequent transients before returning to their baseline fluorescence (Figure 3A).

The total amount of intracellular Ca^{2+} increase generated in each ASCaTs was examined as area under the curve (Figure 3B) and peak amplitude (Figure 3C). Statistical comparison revealed no significant

difference between WT and APP-KO mice. However, ASCaTs in APP-KO mice displayed longer rise time (~22%, Figure 3D) and longer decay time (~20%, Figure 3E), implying slower kinetics of calcium regulation compared to WT controls. In the next evaluation, we considered different categories of transients distinguishing single isolated events from peaks of different order which occurred along a burst-like transient. Similar to the previous analysis, the total amount of intracellular increase of calcium concentration was still comparable to WT within different peak categories (Figure 3F,G). As well, the APP-KO ASCaTs displayed significantly slower kinetics regardless of the order of appearance as a part of a burst activity (Figure 3H,I).

Taken together our results suggest that in the absence of APP the spontaneous increase of Ca^{2+} in microdomains is still able to reach calcium levels comparable to physiological conditions, but with a significant slower rate. As mentioned before, microdomain activity is often driven by mitochondrial Ca^{2+} buffering (8,10,11) that is responsible for the fine tune of calcium homeostasis in the cytosol. For this reason, we decided to further focus on the effect of APP depletion on astrocytic mitochondria, considering it as a potential actor in the observed dysregulated ASCaTs.

Lack of APP results in a fragmented mitochondrial phenotype

To further address the questions why microdomains and ASCaTs are altered in astrocytes of APP-KO animals, we chose to investigate the phenotype in isolated astrocytes. Thus, we prepared primary astrocyte cultures from WT and APP-KO pups (postnatal day 3) and confirmed the lack of APP in astrocytes from APP-KO animals both by immunohistochemistry (Figure 4A) and western blot analysis (Figure 4B).

We next subjected primary cultures of WT and APP-KO astrocytes to electron microscopy (EM) in order to obtain high resolution micrographs of mitochondria and evaluate the effects of APP depletion in isolated astrocytes. 3D-reconstruction of EM image z-stacks revealed shorter and more fragmented, roundish-shaped mitochondria in APP-KO astrocytes compared to WT (Figure 4C,D). This result is in line with previous evidence that the lack of APP results in Ca^{2+} and ATP dysregulations (13,14,16) and morphological alterations of mitochondria (17) suggesting that APP regulates mitochondrial homeostasis.

The fragmented mitochondrial phenotype in APP-KO can be rescued by reintroduction of APP

We further assessed the effect of APP deficiency in astrocytes by immunostaining against translocase of the outer mitochondrial membrane 20 (TOMM20), which serves as a mitochondrial housekeeping protein. In this way, we visualized mitochondria in cultured astrocytes with confocal microscopy (Figure 5A). Subsequently, we used Fiji particle analysis to classify the mitochondrial morphology based on their covered area into structures such as networks (≥ 8.9 µm²), rods (2.7 - 8.8 µm²) and puncta (0.1 – 2.7 µm²) (21). A colour- coded image was generated to visualize puncta, rods and network (Figure 5B).

147 Under physiological conditions mitochondria maintain a tubular shape, organized into extended network

148 structures (22). Interestingly, our analysis revealed a ~10% decrease of area covered by network-shaped

149 mitochondria together with a ~5% increase of both puncta and rod types in APP-KO astrocytes compared

150 to WT (Figure 5C). The western blot analysis of TOMM20 showed no alteration of total protein levels in

151 APP-KO astrocytes (Figure 5D) implying that the total amount of mitochondria was not changed. Thus,

152 APP-KO astrocytes contain fragmented mitochondrial networks without any loss of mitochondria.

153 Finally, we tested the hypothesis that mitochondria fragmentation is directly dependent on APP

154 expression. Therefore, we transfected APP-KO astrocytes with APP-GFP under the EF1alpha promoter.

155 After 5 days, the cells were fixed and immunohistochemically stained for TOMM20 for morphological

156 investigations. Thereby, the GFP expression enabled us to identify the transfected cells that express APP

157 (Figure 5A). Importantly, after re-introducing full-length APP in APP-KO astrocytes, we observed a

158 rescue of the mitochondrial network phenotype, with mitochondria resembling morphological features as

159 in WT (Figure 5A,B,C).

160

Discussion

162 For long time astrocytes have been considered as passive elements involved in the modulation of neuronal

163 functions. Nowadays their active role in regulating brain network, refining synapses, shaping the

164 extracellular space and modulating the metabolic trafficking of neuro- and gliotransmitters is widely

165 accepted (4,23). The proteolytic cleavage of APP generates the amyloid-β peptide that is a key player in

166 the pathogenesis of AD (1). Hence, the investigation of the physiological function of APP and its cleavage

167 products is of major importance for understanding the disease and for finding potential cures. However,

168 such studies have been mainly confined to neurons. Astrocytes express KPI containing isoforms of APP

169 that are closely associated with pathological amyloid-β deposition (2). Therefore, expanding the

170 knowledge about astrocytic APP is crucial for understanding its function in astrocytes and the

171 consequences for associated neurons. Namely, astrocytes exhibit intracellular Ca^{2+} transients that drive

172 gliotransmitter release important for the modulation of neuronal function (6). In our study we considered

173 the effects of APP depletion on spontaneous *in vivo* Ca^{2+} dynamics of microdomains of astrocytic fine

174 processes that are closely associated with synapses. It is of importance to understand the local function of

175 these microdomains in order to decode the contribution of APP to the communication between astrocytes

176 and neurons (4). Thus, we used membrane-tagged genetically encoded Ca^{2+} indicator for the investigation

177 of astrocytic Ca^{2+} transients in astrocytic fine processes (24). Our results clearly demonstrate that lack of

178 APP affects *in vivo* the conformation of the active microdomains and the dynamics of ASCaTs along the

179 fine processes.

180   Given that Ca^{2+} transients along the fine processes of astrocytes are defined by mitochondria-mediated ion

181   homeostasis (10,14), we hypothesized and investigated possible mitochondria dysfunctions. Consistent

182   with our hypothesis, APP-KO astrocytes exhibited mitochondrial network fragmentation which could be

183   rescued by reintroduction of APP. As a result of the observed mitochondria fragmentation, microdomains

184   are deprived of their main energetic sources and cannot sufficiently support surrounding neuronal activity

185   (8). Therefore we hypothesize that the highly ramified protrusions of astrocytes, where microdomains are

186   located, are not fully functional in APP-KO mice, thus explaining the impairments in synaptic plasticity

187   and gliotransmitter release observed in APP-KO animals (12). Since the observed phenotype was the

188   consequence of APP absence, we investigated putative interaction between APP and mitochondria. We

189   reviewed AD-related studies which identified mitochondria as an APP localization target. APP harbors a

190   mitochondrial targeting signal and forms complexes with the translocase of the outer mitochondrial

191   membrane 40 (TOMM40) and the inner mitochondrial membrane 23 (TIMM23), regulating the

192   translocation of nuclear-encoded proteins into the mitochondria (20,25). We therefore reason that

193   depletion of APP compromises mitochondrial protein translocation affecting mitochondria functions and

194   leading to imbalanced intracellular Ca^{2+} homeostasis. In fact, the mitochondria-associated ER membranes

195   (MAMs) are sites where the APP cleavage product C99, composed of the 99-amino acid carboxyl-

196   terminal APP, accumulates and interferes with the mitochondrial respiratory chain (16). Hence, we

197   speculate that C99 at physiological levels has a function in ensuring ER-mitochondria proximity and thus

198   permitting proper mitochondria functionality. The lack of APP and therefore of C99 would impede this

199   interaction resulting in the aforementioned Ca^{2+} alterations. While the interaction between APP, its

200   cleavage products, and neuronal mitochondria in AD have been addressed (20,27), knowledge about the

201   physiological function of APP in astrocytic mitochondria is limited. This study reports mitochondria

202   fragmentation in APP-KO primary astrocyte cultures that interestingly resembles previous findings in

203   HeLa cells expressing KPI-APP mutants (17). As KPI-containing APP isoforms are primarily expressed in

204   astrocytes (2), we presume that the mitochondrial fragmentation and the consequent ASCaTs alteration in

205   APP-KO mice are mainly an astrocyte-specific feature.

206   In summary, this study provides novel insights into the role of APP as a regulator of mitochondrial

207   network and Ca^{2+} homeostasis in astrocytes, breaking ground for further investigations on APP function in

208   astrocytes that has been neglected for too long.

209

210

211

212   **ACKNOWLEDGMENTS**

Figure Legends

Figure 1: Expression pattern of astrocytic viruses, *in vivo* astrocytic Ca^{2+} imaging setting and analysis procedure. (A) Confocal *ex vivo* images of the expression pattern of membrane (green, left) and somatic (red, middle) associated astrocytic viruses and overlay (right) in the somatosensory cortex. Upper row: overview injection site. Lower row: detailed z-projection of a single astrocyte. Scale bar upper row = 100 µm, scale bar lower row = 10 µm. (B) Experimental setting for 2-photon *in vivo* microscopy under monitored anesthesia and analysis workflow for Ca^{2+} trace extraction from astrocytic microdomain GCaMP activity. Briefly, the background subtraction and z-projections of the image series generates an activity profile (heat map) from which ROIs/microdomains can be determined and further used for trace extraction from the raw image series. Notably, not all ROIs/microdomains are displaying transients (purple ROIs and transients). For analysis only the active microdomains (green ROIs and transients) were considered. Scale bar = 10 µm.

Figure 2: Altered astrocytic microdomain size and occurrence in the cortex of APP-KO mice. Color-coded heat map of astrocyte activity showing ASCaTs frequency from WT (A) and APP-KO (B) somatosensory cortex area extracted active microdomains (right, green encircled). Scale bar = 10 µm. (C) Active microdomain density was decreased in APP-KO mice (Student's t test: $t_{(17)}$=3.53, p<0.005). (D) APP-KO microdomain areas were increased, as shown their averaged size ($t_{(94)}$=3.723, p<0.001) and (E) in their frequency distribution (KS test; D=0.1955, p<0.05). (F) The frequency (ASCaTs/min/domain) was reduced in APP-KO mice ($t_{(17)}$=2.878, p<0,05). *p<0.05, **p<0.01, ***p<0.001.

Figure 3: Altered kinetics of astrocytic calcium transients in the cortex of APP-KO mice. (A) Representative traces from active microdomains of WT (above) and APP-KO (below). The area under the curve (B) and peak amplitudes (C) values were comparable between genotypes. The rise time (D)(Student's t test: $t_{(17)}$=2.24, p<0.05) and decay times (E)($t_{(17)}$=2.118, p<0.05) were significantly increased in APP-KO ASCaTs. When considered as isolated (single peak) or ordered by occurrence along burst transients, both area (F) and amplitude (G) values showed no significant difference between KO and WT. More than a specific peak category, there were a general increase of the rise (H)(two-way ANOVA, genotype main factor, $F_{(1,65)}$=9.92, p<0.01) and the decay time (I) (genotype main factor, $F_{(1,65)}$= 17.26, p<0.001) in the kinetics of the ASCaTs of KO mice. *p<0.05, **p<0.01, ***p<0.001.
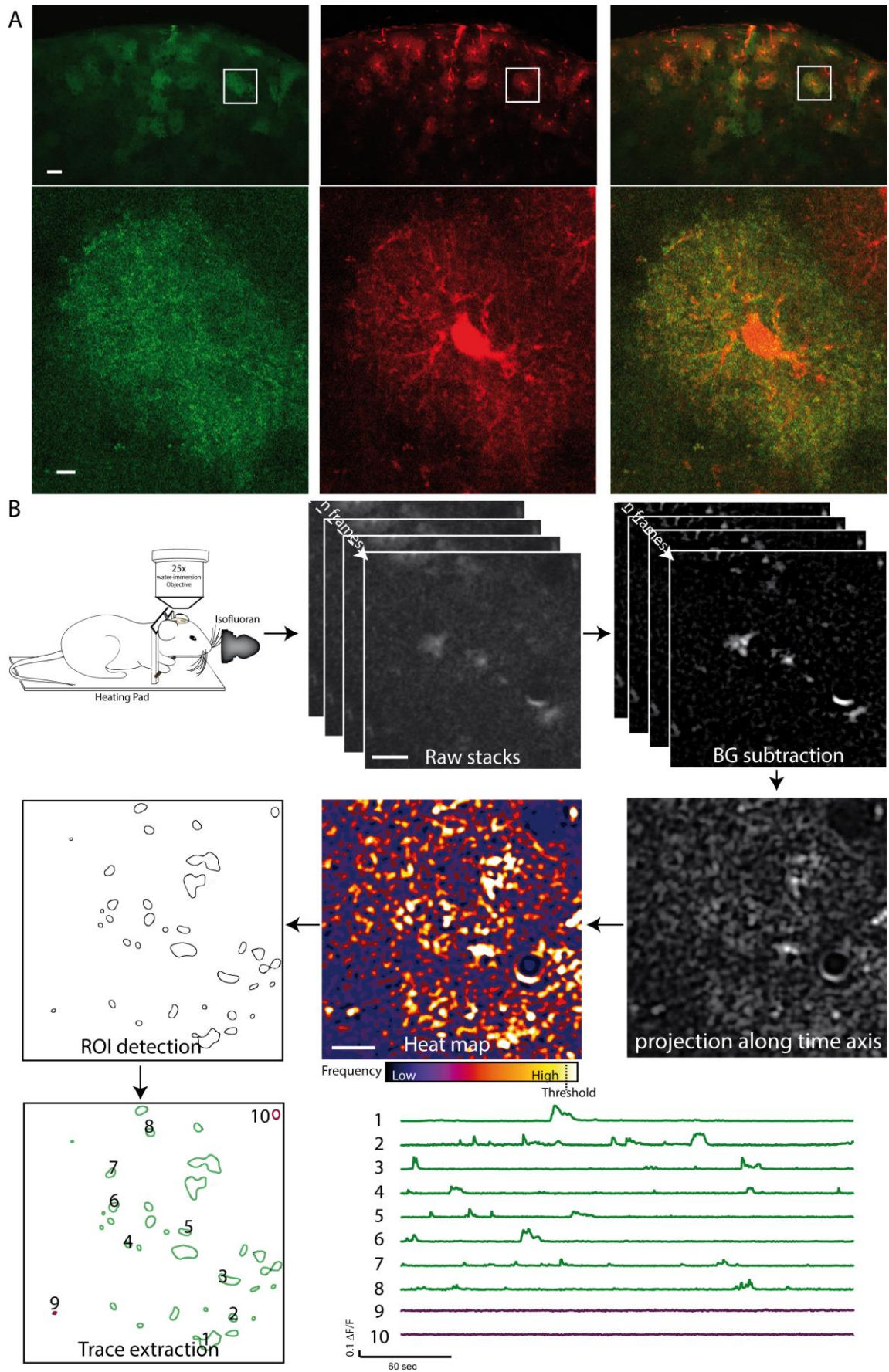
Figure 4: Primary cultured astrocytes lacking APP display fragmented mitochondrial morphology. (A) Immunohistochemical analysis with C-terminus targeted APP antibody on WT (left) and APP-KO (right) primary astrocytes shows exclusive expression of APP in WT. Scale bar = 40 µm. (B) Western blot analysis of primary astrocyte lysates confirms the absence of APP in APP-KO astrocytes with C-terminus targeted APP antibody. Representative FIB/SEM microscopy of WT (C) and APP-KO (D) cultured astrocytes with detailed images of 3D-recontructions (right) illustrate the fragmentation of mitochondria in APP-KO astrocytes. Original FIB/SEM image, scale bar = 2 µm; overview reconstruction (middle), scale bar = 2.5 µm, single mitochondria fragments, scale bar = 1 µm.
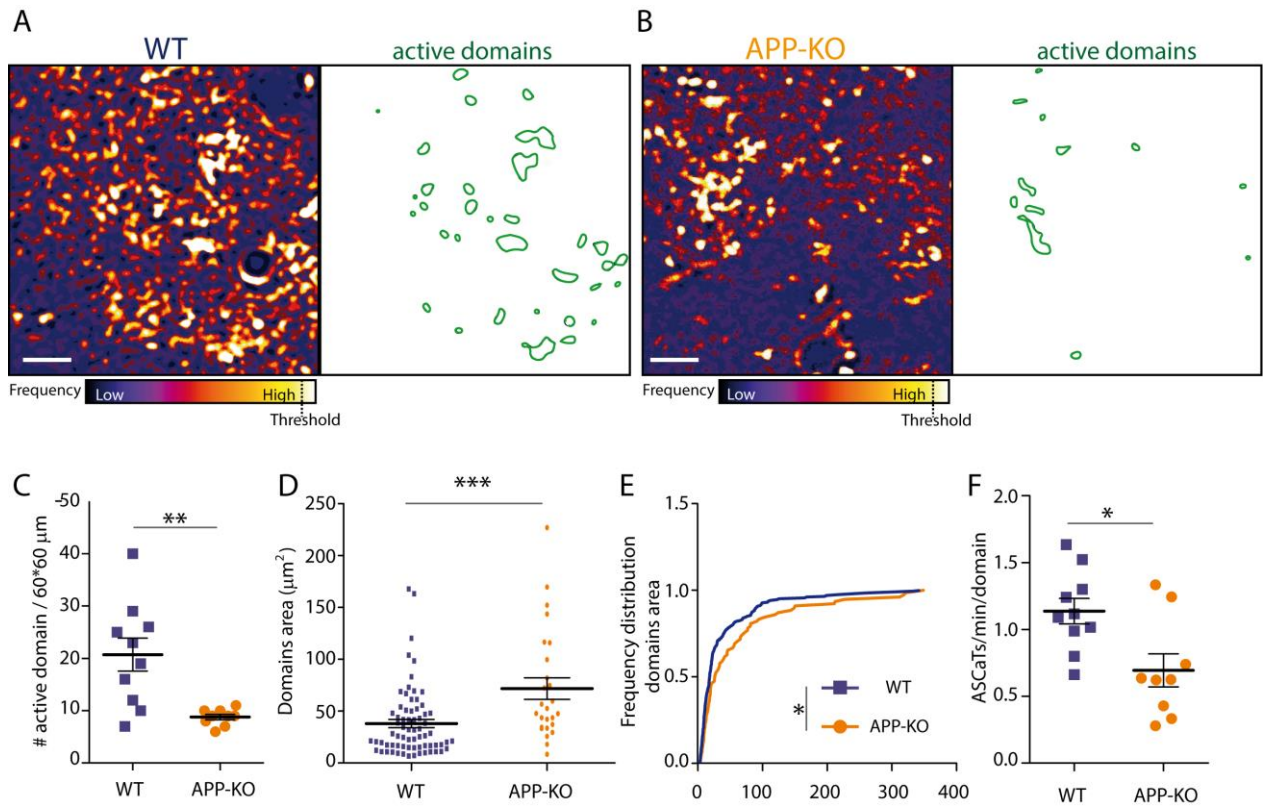
Figure 5: APP-KO astrocytic mitochondria display more fragmented morphology than WT which can be restored by reintroduction of full-length APP. (A) Confocal microscopy images of TOMM20-positive astrocytic mitochondria (in red) from WT, APP-KO and APP-KO + APP-GFP plasmid (in inset). Scale bars = 10µm. (B) Illustrative reconstruction of TOMM20-based morphological classifications: "network" (black), "rods" (green) and "puncta" (red). (C) Quantification of mitochondria morphology. Mitochondria of APP-KO astrocytes were more fragmented compared to WT controls. The reintroduction of full length APP restored physiological composition of mitochondria network in astrocytes. (one-way ANOVA for puncta: $F_{(2,87)}$=21.14, p<0.001; rods: $F_{(2,87)}$=18.38, p<0.001; networks $F_{(2,87)}$=19.78, p<0.001)) (D) Western Blot of TOMM20 and calnexin, (housekeeping protein) and their quantification. TOMM20/calnexin-ratio revealed no difference between WT and APP-KO astrocytes. Bonferroni's post hoc test: ***p<0.001

269   **Figure 1**

270

271
272
273 **Figure 2**

274
275   **Figure 3**

276

WT APP KO

A

B

APP
100 kDa

calnexin
75 kDa

C WT

D APP-KO

277
278
279

Figure 4

A

WT | APP-KO | APP-KO + APP-GFP plasmid

TOMM20

APP-GFP   MERGE

B

Morphological classification

network
rods
puncta

C

D

WT   APP-KO

15 kDa   TOMM20
75 kDa   Calnexin
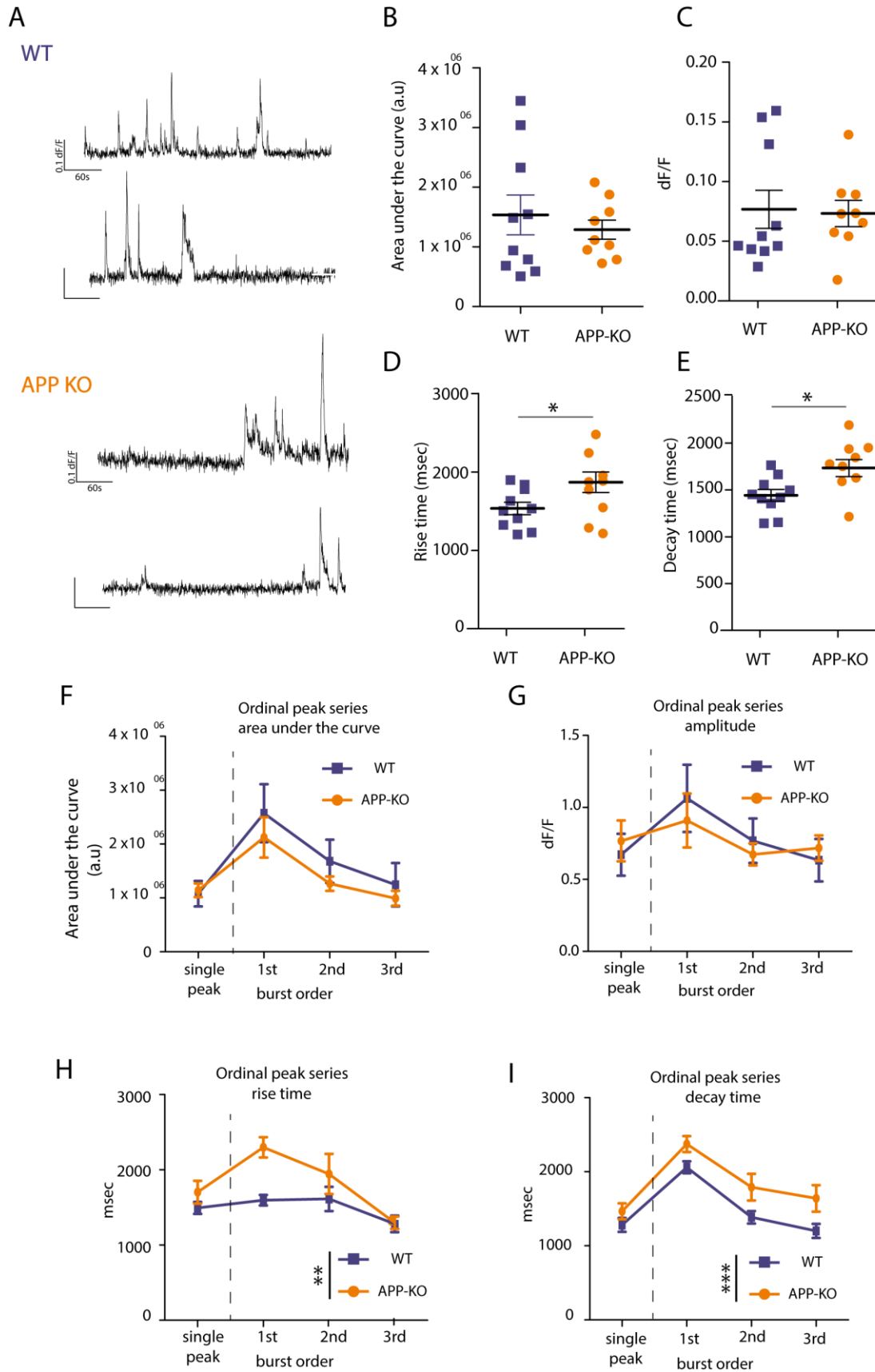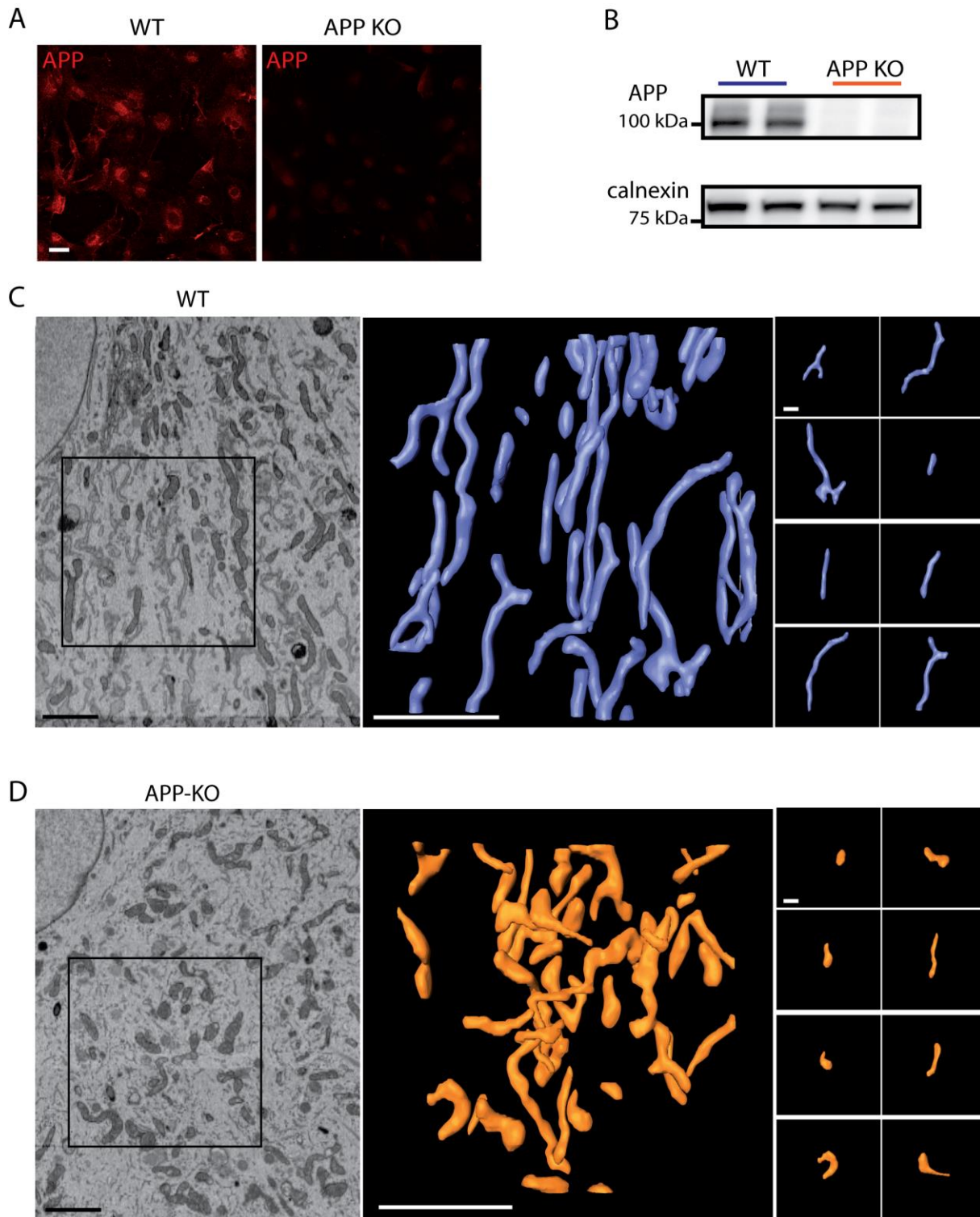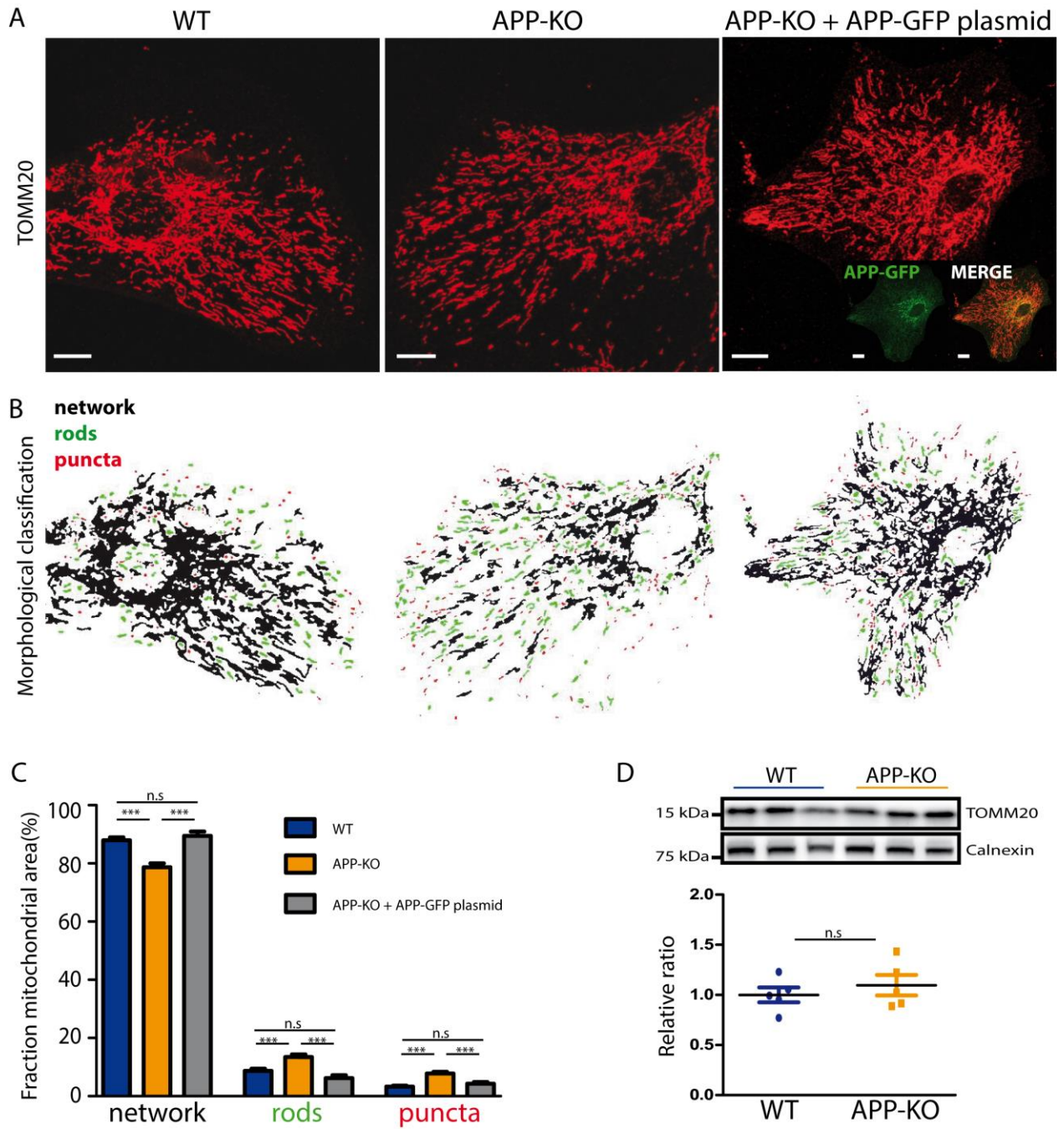
281

282

283   **Figure 5**

284

285

286

287

288

Materials and Methods

Animals

The studies were carried out in accordance with an animal protocol approved by the Ludwig-Maximilians-University Munich and the government of Upper Bavaria (ref. number 55.2-1-54-2532-214-2016). Amyloid precursor protein knock-out (APP-KO) (28,29) and wild type (WT) (C57BL/6) mice as control were used. Mice were group-housed with three to six individuals in standard cages (30 × 15 × 20 cm), with standard bedding and additional nesting material under pathogen-free conditions until surgery. After cranial window implantation they were singly housed in standard cages, with food and water provided ad libitum. Mice were kept under a 12/12-hr light/dark cycle. At the age of 2 months, virus injection and cranial window implantation were performed and at 3 months of age mice underwent in vivo imaging.

Cranial window and viral injection

Details of the cranial window implantation have been previously described (30,31) . Shortly, mice were anesthetized before undergoing surgery by intraperitoneal injection of ketamine/xylazine (respectively 120 and 10 µg/g body weight; WDT/Bayer HealthCare); inflammation and pain were reduced by the subcutaneous administration of the anti-inflammatory drug Rymadil (7.5 µg/g; Pfizer) and the antibiotic Baytril (7 µg/g body weight, Bayer HealthCare). 4 WT and 4 APP KO were injected in three different areas of the somatosensory cortex with: AAV5.GfaABC1D.cyto-tdTomato.SV40 (# 44332, Penn Vector, Philadelphia, PA, USA) and AAV2/5.GfaABC1D.Lck-GCaMP6f (# 52924, Penn Vector, Philadelphia, PA, USA) viruses, in a solution of 10% virus, 45% PBS (1x) and 45% of the original stock of mannitol solution, for a final volume of 300 µl/injection site. Viruses were injected at 200 µm depth from the brain surface with a speed of 30 nl/minute. A piece of skull of the diameter of 4 mm above the somatosensory cortex was removed and a thin glass (VWR International GmbH, Darmstadt, De) was placed on top of the injected area and sealed by dental acrylic (Cyano-Veneer fast; Schein, Vienna, AU). A custom made small metal bar was cemented next to the coverslip to allow head-fixation during imaging sessions.

In vivo Two-Photon Microscopy

Weekly imaging sessions started at earliest 4 weeks after surgery to allow mice to recover and cranial windows to become clear. Mice were anesthetized by isoflurane inhalation (1-1.5% isoflurane in oxygen), head fixed and placed under the microscope. During every imaging session the body temperature was monitored and maintained at 37°C with a thermostat-controlled heating pad. To ensure mice were equally anesthetized during imaging breath rate, oxygen saturation and heart rate were monitored with the Oximeter probe (MouseOx; STARR Life Sciences, Oakmont, PA, USA) and kept constant (breath rate between 60-70 breaths per minute; oxygen saturation between 97% and 98%, and heart rate between 300 and 450 bpm) as suggested in the monitoring protocol (32) . In vivo time-lapse image series of GCaMP6f fluorescence were acquired in the layer 1/2 (120–200 µm below the pial surface) of the somatosensory cortex. Fluorescence image series were collected by the LaVision Trim Scope equipped with tunable Ti:sapphire two-photon lasers (Chameleon, Coherent, Santa Clara, CA, USA) tuned at 940 nm and 25x 1.05 NA water-immersion objective (Olympus, Hamburg, DE). The setup was controlled using LaVision Imspector software (LaVision BioTec GmbH, Bielefeld, DE). Each image frame was acquired at the rate of 4.17 Hz and was 75 x 75 µm with 512 x 512 pixel resolution. Laser power was kept below 20mW. Mice were kept on the stage for a maximum of 1 hour and 30 minutes and during this time period image series from the injected area of the somatosensory cortex were acquired (~8 min per area). Only images

acquired under same anesthesia condition were taken into consideration for astrocytic calcium activity analysis.

Extraction and analysis of Ca²⁺ transients

After an image series was acquired, the x-y axis drift in the image stacks was stabilized using the software Igor 7 Pro (WaveMetrics Inc., Lake Oswego, OR, USA). The protocol used for astrocytic calcium investigation was adapted from the protocol "CASCADE" (11). Calcium transient information about individual microdomain activity was extracted by the combination of custom written codes of Fiji (33) and MiniAnalysis Software (Synaptosoft Inc., Decatur, GA, USA). As a first step, background noise was subtracted by performing 3D convolutions (average and Gaussian filters of size 5x5x5 pixels (x,y,t)) on time-series image stacks $(I(x,y,t))$. By subtracting the products of the average and Gaussian filtering we obtained a noise filtered image stack $(I(x,y,t))$. To identify those regions that exhibit frequent dynamic changes in fluorescence, the mean intensity (avg) and standard deviation (sd) of background pixels noise filtered stacks were calculated. The sum-intensity projected stacks were binarized using a threshold value of avg + 3 sd. By summing the binarized sum- and sd-projected stacks of the noise filtered stack we generated a mask where the core of each microdomain was detected. All domains with an area bigger than 25 pixels were taken into consideration. The binarized mask of the microdomain cores was used as template for ROIs detection. ROIs were finally applied on the raw time series image to plot the GCaMP intensity- levels over the time. Time traces of fluorescence intensity were extracted from the ROIs and converted to dF/F values. We analyzed spontaneous events that occurred in recording session of 300 s. ASCaTs were identified based on amplitudes that were at least 1.5-fold above the baseline noise of the trace (dF/F). Spontaneous events were semi-manually marked, and event amplitudes, area under the curve, time to peak, decay time and event frequency per ROI per min were measured using MiniAnalysis 6.0.07 (Synaptosoft, Inc., Decatur, GA, USA).

Immunofluorescence on brain sections

Mice were anaesthetized with an intraperitoneal injection of ketamine/xylazine (respectively 120 and 10 µg/g body weight; WDT/Bayer HealthCare) and transcardially perfused with phosphate buffered saline (1x PBS) followed by 4% paraformaldehyde in 0.12 M PBS, pH: 7.4. The brain was removed and post-fixed for 24 h at 4°C in the same fixative. The brains were washed in 1x PBS and coronal sections of 50 µm were obtained at room temperature by the vibratome Leica VT 1000S (Leica Mikrosysteme Vertrieb GmbH, Wetzlar, Germany). Immunofluorescence was performed on free floating sections. The study was focused on astrocytes of layer 2/3 of the somatosensory cortex (from bregma 1.98mm to – 1.82mm). Sections were permeabilized (2% TritonX –PBS, Life Science, Darmstadt, DE), gently shacked, overnight at 4°C. Blocking solution (10% normal donkey serum in 1x PBS, Thermo Fisher Scientific Messtechnik GmbH, Munich, DE) was applied for 2 h at room temperature (RT). Sections were incubated with anti-GFP antibody conjugated with Alexa 488 (#A21311, Thermo Fisher Scientific Messtechnik GmbH, Munich, DE) diluted in 3% normal donkey serum, 0,03% Triton-X, 0,05% sodium azide – 1x PBS overnight at 4°C. Brain sections were mounted on polysine slides with Dako Fluorescente Mounting Medium (#S3023, Thermo Fisher Scientific Messtechnik GmbH, Munich, DE). Confocal images were acquired using a Zeiss LSM 780 with a Plan Apochromat 40x/ NA 1.4 Oil DIC M27 with a Pinhole set to 1 airy unit. For a list of all the primary antibodies see below.

Primary cortical astrocyte culture

371   Primary cortical astrocyte cultures were prepared on postnatal day 3 (P3) from APPKO and C57/Bl6
372   animals. The brain was isolated and placed in HBSS (Gibco, cat. 24020091, Thermo Fisher Scientific) at
373   RT. Meninges were removed and the cortex was dissected. Cortices from 3 animals were pooled, cut into
374   pieces, washed with HBSS, and digested in 5 ml Trypsin containing 0.05% EDTA (Gibco; cat. 25300062,
375   Thermo Fisher Scientific) at 37°C for 15 min. The reaction was stopped by adding 5 ml of medium (MEM
376   (Gibco cat. 31095029, Thermo Fisher Scientific), 0.6% Glucose (Merck # 1083371000, CAS 50-99-7),
377   5% heat-inactivated FBS (PAN Biotech P40-37500)). After washing with HBSS, cells were mechanically
378   dissociated in culture medium to obtain a single-cell suspension and plated on a T-75 flask (Nunc EasY
379   Flask cat. 156499, Thermo Fisher Scientific). The medium was changed the next day in order to remove
380   unattached cells. Cultures were grown in an incubator with humid environment at 37°C and 5% CO2
381   (Hereaus, HERAcell 150i). Astrocytic cultures were split at 90% confluency by transferring the cells
382   equally in T-175 flasks (Nunc EasY Flask cat.159910, Thermo Fisher Scientific).

383   Astrocyte culture on coverslips for transfection and immunofluorescence experiments

384   During the second passaging cells were plated on 15 mm glass coverslips (Marienfeld, pretreated
385   overnight (o/n) with nitric acid (Merck), washed with H2O, and sterilized in an oven (Memmert UF30) in
386   a 12 well plate (Nunc cat. 150628, Thermo Fisher Scientific) at a density of 70 000 cells per well. 72 h
387   after plating, cells were transfected with 1µg plasmid carrying APP full length with a C-terminal-GFP-tag
388   under the EF1alpha promoter (peak12/HA-APP-GFP: the insert: EF1a/HA-humanAPP-GFP was cloned
389   into a peak12/RFP backbone using the cloning sites 1: Hind3 and 2: Not1) and 1.5 µl lipofectamine
390   (lipofectamine 2000 reagent, Invitrogen) in OptiMEM (Gibco, cat. 51985026, Thermo Fisher Scientific) +
391   2.5% FBS per well. Astrocytes were incubated with the transfection mix and the medium was changed the
392   following day. Day 5 after transfection cells were washed with autoclaved phosphate-buffered saline (1x
393   PBS) and fixed for 15 min with 4% PFA (Merck, 4% PFA (w/v) in PBS) at RT. After washing with 1x
394   PBS, cells were used for immunofluorescent staining.

395   Western blots of cortical astrocytes culture

396   Westernblot analysis was performed with 2x passaged astrocyte cultures.5 cultures prepared from 3 pups
397   each were taken to obtain 5 biological replicates. After cells reached 90 % confluency they were detached
398   by trypsinization and lysed with STET buffer (50 mM Tris (pH 7.5), 150 mM NaCl, 2 mM EDTA, 1%
399   Triton-X-100,) containing 1:100 freshly added protease inhibitor (P8340, Sigma-Aldrich Chemie Gmbh
400   Munich, De) and 1:100 phosphatase inhibitor (#5870 Cell signaling) for 30 min on ice. Protein
401   concentration was determined with bicinchoninic acid (BCA) assay (Uptima Interchim) and samples were
402   mixed 1 in 4 with 4x Laemmli buffer (8% SDS, 40% Glycerol, ~0.025% Bromophenol blue, 10% β-
403   mercaptoethanol, 125 mM Tris, pH 6.8). 10-15 µg protein was loaded on a gradient gel (M42015,
404   Genscript ExpressPlus PAGE gel 4-20%) and SDS-PAGE was performed with Tris-MOPS-SDS Buffer
405   (M00138, Genscript,). Proteins were transferred onto a PVDF membrane (IPVH 00010, Merck) in transfer
406   buffer (25 mM Tris, 240 mM Glycin, 10% Methanol). The membrane was blocked with 5% skim milk
407   (Sigma-Aldrich Chemie Gmbh Munich, De) in PBS-T (1x Phosphate buffered saline + 0.05% Tween) for
408   at least 30 min at RT with horizontal rotation. After washing with PBS-T following antibodies were used
409   for WB analysis: primary antibodies in PBS-T, 0.25% BSA and incubated o/n at 4°C APPY188 1:1000,
410   TOMM20 1:1000 (see antibody list), 1h at RT β-actin 1:10000 (A5316, clone AC-74, Sigma), 1 h at RT
411   calnexin 1:10000 (ADI-SPA-860, Enzo); secondary antibodies in PBS-T, 0.25% BSA and incubated 1h at
412   RT anti-mouse- horseradish peroxidase (HRP) 1:10000 (Promega, Mannheim, De), anti-rabbit-HRP

413   1:10000 (Promega). Protein signals were developed with enhanced chemiluminescence (ECL) (ECL-
414   substrate, GE Healtcare) and visualized using ImageQuant LAS4000 (GE Healthcare).

Immunofluorescence on cortical astrocyte culture

416   Cover glasses were placed into a humid chamber, quenched for 10 minutes with 50 mM Ammonium
417   Cloride and extracted with 0.1% Triton-X 1x PBS (Life Science, Darmstadt, Germany) for 3 minutes at
418   RT. To prevent unspecific binding, a 10 % blocking solution (2% FCS, 2% BSA, 0.2% fish Gelatin)
419   diluted in 1x PBS was applied on the coverslips for 1 h at room temperature. For immunolabelling
420   sections were incubated 1 h at RT with primary antibody diluted in 10% blocking solution/ PBS (for a
421   complete primary antibodies list see table). After rinsing the coverslips 3 times with 1x PBS we applied
422   secondary antibodies diluted in 10% blocking solution/ PBS. The secondary antibodies applied, raised in
423   goat or donkey, were: Alexa 594, Alexa 488, and Alexa 647 diluted 1:500 in 10% blocking solution/PBS.

FIB/SEM characterization of mitochondria morphology

425   During the second passaging, primary cortical astrocytes were plated on 15 mm glass coverslips
426   (Marienfeld , pretreated overnight (o/n) with nitric acid (Merck) and sterilized) in a 12 well plate (Nunclon
427   delta surface) at a density of 70 000 cells per well. After 5 days, astrocytes were rinsed with autoclaved
428   phosphate buffered saline) briefly and fixed with 2,5% glutardialdehyde in cacodylate-buffer (75 mM
429   cacodylate, 75 mM NaCl, 2 mM MgCl2) for 30 min, followed by 3 washing steps in cacodylate buffer.
430   Thereafter, cells were post-fixed with 1% OsO4 and 1% K4Fe(CN)6 in cacodylate buffer for 30 min,
431   washed 3 times in ddH2O, incubated with 1% thiocarbohydrazide in ddH2O for 30 minutes, washed with
432   ddH2O 3 times, followed by a second post-fixation with 1% OsO4 in ddH2O for 30 min. Samples were
433   further rinsed 3 times with ddH2O, dehydrated in a graded series of acetone (10%, 20%, 40%, 60%, 80%,
434   100%, 100%, 100%; 10 min each) including an incubation step in 1% uranyl acetate in 20 % acetone for
435   30 min. Subsequently, cells were infiltrated and embedded as described previously (34). Tomographic
436   datasets were obtained by the 'slice and view' technique using a Zeiss Auriga 40 crossbeam workstation
437   (Carl Zeiss Microscopy, Oberkochen, DE). For milling with the Ga-ion beam, the conditions were as
438   follows: 0.5–1 nA milling current of the Ga-emitter; with each step 50 nm of the epoxy resin was
439   removed. SEM images were recorded at 1.5 kV with an aperture of 60 μm operated in the high current
440   mode with the in-lens EsB detector (EsB grid set to −1000 V). The voxel size was 5 nm in x/y and 50 in z.
441   FIB/SEM image stacks were aligned, segmented and 3D reconstructed with Amira® (Thermo Fischer
442   Scientific Messtechnik GmbH, Munich, DE).

Mitochondria morphological investigation

444   Mitochondria of cultured astrocytes were stained against TOMM20 (see table for protocol) and mounted
445   with Dako Fluorescent Mounting Medium (S3023) on Polysine slides (Thermo Scientific, P4981). Z-
446   stacks confocal microscopy images were acquired (x: 106.07 μm, y: 106.07 μm, z: between 3-6 μm, 0.5
447   μm interval; Zeiss 40x/1.4, oil immersion) and 2-D deconvoluted (AutoQuantX3, Media Cybernetics).
448   Projection on the z-axis was performed to obtain a single in-focus field projection. Mitochondria were
449   selected by thresholding the pictures and processing them using the software Fiji (33). Classification of
450   mitochondria morphology in network, rods and puncta was done accordingly to the following values:
451   puncta area: $0.1 - 2.7$ μm²; rods area: $2.7 - 8.8$ μm² and network area: from 8.9 μm². Based on the area
452   covered by the mitochondria, a colour- coded image was generated to visualize in red puncta, in green
453   rods and in blue the network. GFP signal of APP-GFP transfected cells was amplified by anti-GFP

staining which allowed visual identification and investigation of their mitochondria. For statistical analysis the morphological class is shown as fraction (%) of the total mitochondria area (TOMM20) of an astrocyte, n = 30 astrocytes.

Statistical analysis

For statistical analysis and comparisons GraphPad Prism 5.04 (GraphPad Software, Inc., La Jolla, CA USA) was used. For each set of data, we determined whether values were normally distributed or not. If they were normally distributed, we used parametric tests; otherwise, we used non-parametric tests (unpaired two-tailed Student's t test and two-way ANOVA followed by Bonferroni post-hoc test or Mann Whitney test). For frequency distribution comparison, Kolmogorov-Smirnov test was applied. P-value < 0.05 was defined as statistically significant. All the analysis was performed blinded with respect to mouse genotype.

Primary Antibody list for Immunofluorescence

ANTIGEN	SOURCE	TYPE	DILUTION FACTOR	INCUBATION	SAMPLE
GFP-Alexa conjugated488	Thermo Fisher (#A21311)	rb	1:500	2 h /room temp.	Brain slice, astrocytic culture
TOMM20 **Mitochondrial import receptor**	Abcam (#186735)	rb	1:200	1 hour/ room temp.	Astrocytic culture
APPY188 **Amyloid Precursor Protein**	Abcam (#32136)	rb	1:200	1 hour/ room temp.	Astrocytic culture

References

475

476 1.   Müller UC, Deller T, Korte M. Not just amyloid: physiological functions of the amyloid precursor
477 protein family. Nat Rev Neurosci. 31. März 2017;18(5):281–98.

478 2.   Rohan de Silva HA, Jen A, Wickenden C, Jen L-S, Wilkinson SL, Patel AJ. Cell-specific expression of
479 β-amyloid precursor protein isoform mRNAs and proteins in neurons and astrocytes. Mol Brain Res. 1.
480 Juli 1997;47(1):147–56.

481 3.   Haass C, Hung AY, Selkoe DJ. Processing of beta-amyloid precursor protein in microglia and
482 astrocytes favors an internal localization over constitutive secretion. J Neurosci. 1. Dezember
483 1991;11(12):3783–93.

484 4.   Perea G, Navarrete M, Araque A. Tripartite synapses: astrocytes process and control synaptic
485 information. Trends Neurosci. August 2009;32(8):421–31.

486 5.   Kimelberg HK, Nedergaard M. Functions of astrocytes and their potential as therapeutic targets.
487 Neurotherapeutics. 2010;7(4):338–353.

488 6.   Martineau M, Parpura V, Mothet J-P. Cell-type specific mechanisms of D-serine uptake and
489 release in the brain. Front Synaptic Neurosci. 2014;6:12.

490 7.   Shigetomi E, Bowser DN, Sofroniew MV, Khakh BS. Two Forms of Astrocyte Calcium Excitability
491 Have Distinct Effects on NMDA Receptor-Mediated Slow Inward Currents in Pyramidal Neurons. J
492 Neurosci. 25. Juni 2008;28(26):6659–63.

493 8.   Grosche J, Matyash V, Möller T, Verkhratsky A, Reichenbach A, Kettenmann H. Microdomains for
494 neuron–glia interaction: parallel fiber signaling to Bergmann glial cells. Nat Neurosci. 1999;2(2):139–143.

495 9.   Rizzuto R, De Stefani D, Raffaello A, Mammucari C. Mitochondria as sensors and regulators of
496 calcium signalling. Nat Rev Mol Cell Biol. 1. August 2012;13(9):566–78.

497 10.   Srinivasan R, Huang BS, Venugopal S, Johnston AD, Chai H, Zeng H, u. a. Ca2+ signaling in
498 astrocytes from Ip3r2 −/− mice in brain slices and during startle responses in vivo. Nat Neurosci. Mai
499 2015;18(5):708–17.

500 11.   Agarwal A, Wu P-H, Hughes EG, Fukaya M, Tischfield MA, Langseth AJ, u. a. Transient Opening of
501 the Mitochondrial Permeability Transition Pore Induces Microdomain Calcium Transients in Astrocyte
502 Processes. Neuron. Februar 2017;93(3):587–605.e7.

503 12.   Zou C, Crux S, Marinesco S, Montagna E, Sgobio C, Shi Y, u. a. Amyloid precursor protein
504 maintains constitutive and adaptive plasticity of dendritic spines in adult brain by regulating D?serine
505 homeostasis. EMBO J. 17. Oktober 2016;35(20):2213–22.

506 13.   Linde CI, Baryshnikov SG, Mazzocco-Spezzia A, Golovina VA. Dysregulation of Ca2+ signaling in
507 astrocytes from mice lacking amyloid precursor protein. AJP Cell Physiol. 1. Juni 2011;300(6):C1502–12.

508   14.   Hamid R, Kilger E, Willem M, Vassallo N, Kostka M, Bornhövd C, u. a. Amyloid precursor protein
509   intracellular domain modulates cellular calcium homeostasis and ATP content. J Neurochem. 1. August
510   2007;102(4):1264–75.

511   15.   Jackson JG, Robinson MB. Reciprocal Regulation of Mitochondrial Dynamics and Calcium
512   Signaling in Astrocyte Processes. J Neurosci. 11. November 2015;35(45):15199–213.

513   16.   Pera M, Larrea D, Guardia-Laguarta C, Montesinos J, Velasco KR, Agrawal RR, u. a. Increased
514   localization of APP-C99 in mitochondria-associated ER membranes causes mitochondrial dysfunction in
515   Alzheimer disease. EMBO J. 15. November 2017;36(22):3356–71.

516   17.   Wang Y, Wu F, Pan H, Zheng W, Feng C, Wang Y, u. a. Lost region in amyloid precursor protein
517   (APP) through TALEN-mediated genome editing alters mitochondrial morphology. Sci Rep. 29. Februar
518   2016;6:srep22244.

519   18.   Del Prete D, Suski JM, Oulès B, Debayle D, Gay AS, Lacas-Gervais S, u. a. Localization and
520   Processing of the Amyloid-β Protein Precursor in Mitochondria-Associated Membranes. Ghribi O,
521   Herausgeber. J Alzheimers Dis. 20. Dezember 2016;55(4):1549–70.

522   19.   Anandatheerthavarada HK, Biswas G, Robin M-A, Avadhani NG. Mitochondrial targeting and a
523   novel transmembrane arrest of Alzheimer's amyloid precursor protein impairs mitochondrial function in
524   neuronal cells. J Cell Biol. 14. April 2003;161(1):41–54.

525   20.   Devi L, Prabhu BM, Galati DF, Avadhani NG, Anandatheerthavarada HK. Accumulation of Amyloid
526   Precursor Protein in the Mitochondrial Import Channels of Human Alzheimer's Disease Brain Is
527   Associated with Mitochondrial Dysfunction. J Neurosci. 30. August 2006;26(35):9057–68.

528   21.   Leonard AP, Cameron RB, Speiser JL, Wolf BJ, Peterson YK, Schnellmann RG, u. a. Quantitative
529   analysis of mitochondrial morphology and membrane potential in living cells using high-content imaging,
530   machine learning, and morphological binning. Biochim Biophys Acta BBA - Mol Cell Res. Februar
531   2015;1853(2):348–60.

532   22.   Rafelski SM. Mitochondrial network morphology: building an integrative, geometrical view. BMC
533   Biol. 24. Juni 2013;11(1):71.

534   23.   Haber M. Cooperative Astrocyte and Dendritic Spine Dynamics at Hippocampal Excitatory
535   Synapses. J Neurosci. 30. August 2006;26(35):8881–91.

536   24.   Shigetomi E, Bushong EA, Haustein MD, Tong X, Jackson-Weaver O, Kracun S, u. a. Imaging
537   calcium microdomains within entire astrocyte territories and endfeet with GCaMPs expressed using
538   adeno-associated viruses. J Gen Physiol. Mai 2013;141(5):633–47.

539   25.   Pagani L, Eckert A. Amyloid-Beta Interaction with Mitochondria. Int J Alzheimers Dis.
540   2011;2011:925050.

541   27.   Spuch C, Ortolano S, Navarro C. New Insights in the Amyloid-Beta Interaction with Mitochondria.
542   J Aging Res. 2012;2012:324968.

543   28.   Magara F, Müller U, Li Z-W, Lipp H-P, Weissmann C, Stagljar M, u. a. Genetic background changes
544   the pattern of forebrain commissure defects in transgenic mice underexpressing the β-amyloid-
545   precursor protein. Proc Natl Acad Sci. 1999;96(8):4656–4661.

546   29.   Ring S, Weyer SW, Kilian SB, Waldron E, Pietrzik CU, Filippov MA, u. a. The Secreted ?-Amyloid
547   Precursor Protein Ectodomain APPs? Is Sufficient to Rescue the Anatomical, Behavioral, and
548   Electrophysiological Abnormalities of APP-Deficient Mice. J Neurosci. 18. Juli 2007;27(29):7817–26.

549   30.   Fuhrmann M, Mitteregger G, Kretzschmar H, Herms J. Dendritic Pathology in Prion Disease Starts
550   at the Synaptic Spine. J Neurosci. 6. Juni 2007;27(23):6224–33.

551   31.   Holtmaat A, Bonhoeffer T, Chow DK, Chuckowree J, De Paola V, Hofer SB, u. a. Long-term, high-
552   resolution imaging in the mouse neocortex through a chronic cranial window. Nat Protoc. August
553   2009;4(8):1128–44.

554   32.   Ewald AJ, Werb Z, Egeblad M. Monitoring of vital signs for long-term survival of mice under
555   anesthesia. Cold Spring Harb Protoc. 2011;2011(2):pdb–prot5563.

556   33.   Schindelin J, Arganda-Carreras I, Frise E, Kaynig V, Longair M, Pietzsch T, u. a. Fiji: an open-source
557   platform for biological-image analysis. Nat Methods. Juli 2012;9(7):676–82.

558   34.   Gaertner F, Ahmad Z, Rosenberger G, Fan S, Nicolai L, Busch B, u. a. Migrating Platelets Are
559   Mechano-scavengers that Collect and Bundle Bacteria. Cell. November 2017;171(6):1368–1382.e23.

560